mater.scichina.com link.springer.com

Published online 9 May 2023 | https://doi.org/10.1007/s40843-023-2431-3
Sci China Mater 2023, 66(8): 3310–3318

Hierarchical porous carbon nanofibers for highly efficient solar-driven water purification

Qingliang Luo[1], Yi Yang[1], Kangkang Wang[1], Jianyong Yu[2], Rongwu Wang[1*], Dongxiao Ji[1*] and Xiaohong Qin[1]

ABSTRACT **Carbon materials are commonly used in the solar steam generation because they can absorb broadband light and generate heat effectively. However, conventional carbon with a smooth surface is limited by a moderate reflection of approximately 10%, causing significant reflective energy loss. Thus, we proposed a nanoscale multiple interface strategy to boost the intrinsic light absorption of carbon nanofibers (CNFs) for more efficient solar-driven water purification. The multiple interfaces were constructed by introducing hierarchical nanopores in CNFs (HPCNFs) through a facile sacrificial framework method. Owing to the high surface roughness and abundant internal air-dielectric interfaces derived from the hierarchical pores, the HPCNFs show significant improvement in broadband light (300–2500 nm) absorption up to 97.62%, which enables high solar-vapor conversion efficiency of 96.13% and evaporation rate of 1.78 kg m^{-2} h^{-1} under one sun illumination, surpassing majority of the related carbon materials. When used for solar steam desalination, the HPCNF film demonstrates high rejection of ions (< 0.05 mg L^{-1} salt ions) and produces freshwater from the lake at a rate of 11.18 kg m^{-2} per day, adequate to satisfy the daily needs of 4–5 individuals. This work provides a facile strategy for designing efficient carbon-based solar steam generation materials.**

Keywords: multiple interfaces, carbon nanofibers, electrospinning, solar-vapor generation, water purification

INTRODUCTION

The global shortage of clean water is affecting a large number of people worldwide [1,2]. Extracting fresh water from natural water sources is an important method to alleviate this crisis [3,4]. Solar steam generation technology is regarded as an eco-friendly strategy for water purification owing to its low cost and low power consumption [5,6]. This technology uses materials with high light absorption properties and converts light into heat energy, which is then used to obtain pure water vapor. Therefore, photothermal materials are core to realizing solar-steaming technology.

Currently, metal/metal oxides [7–9], semiconductors [10], hydrogels [11], and carbon-based materials [12,13] have been explored as efficient photothermal elements in solar-steaming systems. The development of carbon-based materials is rapid in this area owing to their easy availability, high chemical stability, and good light absorption properties. A solar power generation system made of chitosan and reduced graphite oxide, which was reported by Wang *et al.* [14], can achieve a water evaporation rate of 1.44 kg m^{-2} h^{-1} with an evaporation efficiency of 87% under one sun. Ma *et al.* [15] constructed an interpenetrating network for solar-vapor generation using single-walled carbon nanotubes as threads and achieved a water evaporation rate of 1.38 kg m^{-2} h^{-1} and solar-vapor generation efficiency of 90.8% under one sun. Carbon black [16], biochar [17], and carbon nanofibers (CNFs) [18] exhibit similar performance. Current research has gradually shifted to building various complex three-dimensional (3D) structures using carbon materials to further enhance the solar-vapor conversion efficiency, such as double-layer wooden structure evaporator [19] and graphene oxide-based aerogel [20]. However, few studies have focused on improving the intrinsic solar steam generation performance of carbon materials. Owing to the reflection on the smooth surface of carbon [21], the carbon materials have limited absorption of approximately 90%, causing significant reflective energy loss [22].

According to the law of refraction, when light repeatedly passes through the air-dielectric interface, the light gets trapped in the nanostructures and subsequently absorbed by multiple internal reflections [23]. Herein, we proposed a multiple interface strategy to boost the intrinsic light absorption of CNFs for more efficient solar-driven water purification. CNFs have a large specific surface area and good mechanical properties, applicable to various scenarios [23]. The zeolite imidazolate framework-8 (ZIF-8) is a commonly used pore-making template with excellent dimensional accuracy [24]. We employed ZIF-8 and polyacrylonitrile (PAN) for electrospinning to fabricate nanofiber precursors, which were then pyrolyzed to obtain porous CNFs with a rough surface and rich air-dielectric interface inside the fiber. The optical path length increases significantly in the resulting CNF network, enabling the fiber network to exhibit superior broadband light (300–2500 nm) absorption of 97.62%. This helps achieve a high water evaporation rate of 1.78 kg m^{-2} h^{-1} under one sun. This value surpasses many carbon materials with complex 3D spatial structures [25]. The fabricated rough CNF membrane can be directly used for practical outdoor solar steam water purification. It demonstrates a high rejection rate of ions (< 0.05 mg L^{-1} salt ions) and purifies fresh water from the lake at a rate of 11.18 kg m^{-2} per day. This

[1] Key Laboratory of Textile Science and Technology of Ministry of Education, College of Textiles, Donghua University, Shanghai 201620, China
[2] Innovation Center for Textile Science and Technology, Donghua University, Shanghai 201620, China
[*] Corresponding authors (emails: jidongxiao@dhu.edu.cn (Ji D); wrw@dhu.edu.cn (Wang R))

performance is sufficient for the daily demands of 4–5 individuals.

EXPERIMENTAL SECTION

Materials

PAN (*M*w = 130,000) was obtained from Sigma-Aldrich. *N*,*N*-dimethylformamide (DMF, analytical reagent (AR), ≥ 99.5%), zinc nitrate hexahydrate ($Zn(NO_3)_2{\cdot}6H_2O$, AR, ≥ 99%), and anhydrous methanol (CH_3OH) were purchased from Sinopharm Chemical Reagent Co., Ltd. (China). 2-Methylimidazole (2-MIM, AR, 98%) was purchased from Aladdin Chemistry Co., Ltd. (Shanghai, China). All chemicals were directly used without any further purification. Deionized water (18.5 MΩ cm^{-1}) was used in all experiments.

Synthesis of ZIF-8

ZIF-8 crystals were synthesized by the reported procedure with some modifications [26]. Briefly, 3 mmol of $Zn(NO_3)_2{\cdot}6H_2O$ and 20 mmol of 2-MIM were dissolved in 30 and 20 mL of methanol with magnetic stirring at room temperature, respectively. The two solutions were mixed and stirred for 2 min before being left undisturbed at room temperature for 24 h. The precipitate was centrifuged and washed thrice with methanol to remove the residual precursor before being vacuum dried at 40°C for 24 h. The average particle size of the obtained ZIF-8 was approximately 100 nm (Fig. S1). The preparation process for another size of ZIF-8 was similar to the abovementioned method, except that the amount of all chemical reagents was increased tenfold. The obtained ZIF-8 had an average size of 50 nm (Fig. S2).

Preparation of rough CNFs

We dispersed 0.6 g of 50-nm ZIF-8 nanoparticles in 6 mL of DMF by sonicating for 1.5 h. Then, 0.4 g of PAN powder was added to the ZIF-8 dispersion and continuously stirred for 4 h at 60°C to yield a homogenous spinning solution. The spinning solution was electrospun on aluminum foil substrates for 16 h at 9.5 kV, a flow rate of 0.2 mL h^{-1}, and a spin distance of 12 cm. The temperature and relative humidity were maintained at 25°C and 30% ± 5%, respectively. The as-spun PAN/ZIF-8 nanofibers were carbonized at 550°C in N_2 for 1 h with a heating rate of 3°C min^{-1}, then carbonized at 950°C under N_2 for 2 h with a heating rate of 5°C min^{-1} to obtain CNFs (HRCNFs) with higher roughness and rich air-dielectric interfaces inside the fibers (characterized by Brunauer-Emmett-Teller (BET) specific surface area). The nanofiber surface exhibited lower roughness CNF (LRCNF) and less air-dielectric interfaces when using 100-nm ZIF-8 nanoparticles compared with those with 50-nm ZIF-8 nanoparticles.

The smooth CNFs were prepared using pure PAN with the same procedure, and the corresponding CNFs were named CNF.

Characterizations

The morphologies of the materials were determined *via* transmission electron microscopy (TEM, JEOL JEM-2010F) and field emission scanning electron microscopy (Regulus8230, Hitachi, Japan). High-angle annular dark-field scanning TEM (HAADF-STEM) images, STEM mapping, and line-scan energy-dispersive X-ray spectra were captured using STEM (Tecnai G2 F30S-Twin, Philips-FEI). Surface morphologies and roughness of the nanofibers were measured by using atomic force microscopy (AFM, Bruker Dimension Icon, USA) in the tapping mode. The thickness of the samples was tested with a thickness gauge (YG141N, Nantong Hongda Instruments Co., Ltd., China). The thicknesses of HRCNF, LRCNF, and CNF were 78, 79, and 77 μm, respectively. BET was used at liquid nitrogen temperature to measure the N_2 adsorption/desorption isotherms of the samples with a physisorption analyzer (Autosorb-Iq, U.S.). The diameter distribution of fibers was calculated using ImageJ software (NIH, America) by measuring a minimum of 100 fibers. An ultraviolet-visible-near-infrared (UV-vis-NIR) spectrometer (Shimadzu, UV-3600, Japan) with an integrating sphere was used to assess the solar transmittance and reflectance of the materials. Inductively coupled plasma-atomic emission spectrometry was used to measure the ion concentration (ICP-715-AES instrument, Varian, USA).

Solar steam generation experiments

The steam generation experiment was performed using a solar simulator (Sun-500, Beijing CEAULIGHT Technology Co., Ltd., China) equipped with an optical filter for the typical AM 1.5 sun spectrum. The power density of the irradiation of the solar light was measured using a solar power meter (CEL-FZ-A, Beijing CEAULIGHT Technology Co., Ltd., China). The weight loss and weight of the collected clean water were measured using an electronic balance (FA 2004, LICHEN Technology Co., Ltd., China) with an accuracy of 0.0001 g. An IR thermal camera was used to record the surface temperature of the sample (Fotric 226, China). The sample was cut into a circular membrane with a diameter of 3.5 cm and attached to a round polystyrene foam tightly wrapped in cotton filter paper, with the excess filter paper immersed in salt water along the foam edge to evaluate the solar evaporation performance. The entire structure was allowed to float on top of a 100-mL beaker of salt water.

The solar absorption (α) of the samples was calculated using [27]

$$\alpha = \int_{\lambda_{\min}}^{\lambda_{\max}} \left[1 - \rho_{\lambda}(\lambda)\mathrm{d}\lambda\right] / \int_{\lambda_{\min}}^{\lambda_{\max}} G_{\lambda}(\lambda)\mathrm{d}\lambda, \quad (1)$$

where ρ_{λ} (%) represents light reflectivity and G_{λ} (W m^{-2} nm^{-1}) represents the wavelength-dependent solar spectral irradiation. λ refers to the wavelength (nm).

The evaporation rate (v) was calculated using [28]

$$v = \mathrm{d}m / s\mathrm{d}t, \quad (2)$$

where m (kg) is the mass change caused by water evaporation. The surface area of the test sample directly exposed to simulated solar light is denoted by s (m^2). The solar illumination time is given by t (h).

To evaluate the evaporation performance of photothermal materials, the solar-vapor conversion efficiency (η_{ep}) was calculated using [29]

$$\eta_{ep} = \frac{mh_{lv}}{p_{in}}, \quad (3)$$

where m is the mass flux, h_{lv} is the total enthalpy of liquid vapor phase change (sensible heat + phase change enthalpy), and p_{in} is the power density of solar illumination (1 kW m^{-2}).

RESULT AND DISCUSSION

A scalable two-step method was used to fabricate the hierarchical porous CNF (Fig. 1a). First, a homogeneous solution

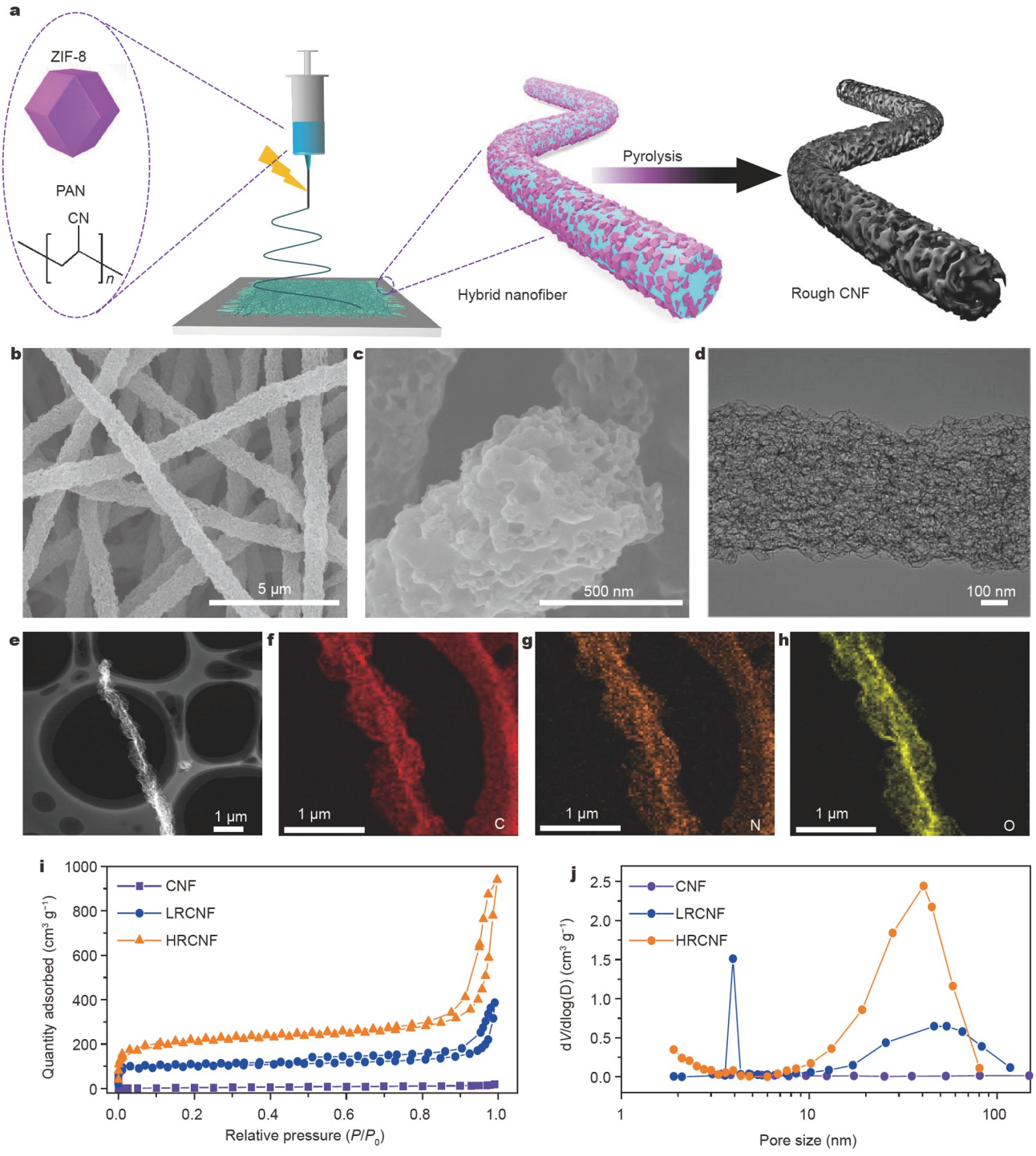

Figure 1 (a) Illustration of the fabrication process of hierarchical porous rough CNF. (b, c) SEM images of HRCNF. (d) TEM image of HRCNF. (e) HAADF-STEM image of HRCNF. (f–h) Corresponding elemental mapping images of HRCNF. (i) N_2 adsorption-desorption isotherms of CNFs, LRCNFs, and HRCNFs. (j) Pore width distributions of CNFs, LRCNFs, and HRCNFs.

containing PAN and ZIF-8 was electrospun into a nanofiber with a diameter centered at 580 nm (Fig. S3). The nanofiber membrane precursor was then subjected to the carbonization step, where the continuous PAN matrix evolved into carbon fiber under high-temperature reduction, and ZIF-8 underwent thermal degradation to form a porous structure in the fiber. The pore generation made the fiber surface rough. The static air stored in the pores forms a large amount of air-dielectric interface with the carbon medium. When the particle size of ZIF-8 becomes smaller, the pores on the fiber surface will increase, and the fiber roughness will increase. For comparison, we used 50- and 100-nm ZIF-8 to prepare carbon fibers with different nanoscale roughnesses, denoted as HRCNF and LRCNF, respectively. The resulting rough, porous CNF membranes had good mechanical properties, such as good flexibility (Fig. S4), which enabled them to be directly applied to practical

applications without further processing.

The SEM image demonstrates that HRCNFs with an average diameter of 524 nm (Fig. S5) formed a staggering network, making the CNF membrane surface uneven, which was beneficial for light absorption (Fig. 1b) [30]. Open mesopores could be observed on the CNF surface (Fig. 1c), and the rough undulation was determined by the pore size. LRCNFs showed a similar staggered nanofiber network structure and rough surface with larger holes on the CNF (Fig. S6). CNFs without ZIF-8 had a smooth fiber surface with an average diameter of 505 nm (Fig. S7). The TEM image (Fig. 1d) reveals abundant macro/mesopores in the nanofibers. The high-angle annular dark-field TEM image and energy-dispersive X-ray spectroscopy (EDX) mapping images of HRCNF reveal that C, N, and O elements are evenly distributed on the porous CNFs (Fig. 1e–h).

The N_2 physical sorption method was used to investigate the structural details of CNFs, LRCNFs, and HRCNFs. CNFs showed a small N_2-based BET surface area of 18.67 $m^2 g^{-1}$. LRCNFs and HRCNFs possessed ultra-high BET-specific surface areas of 382.70 and 755.97 $m^2 g^{-1}$ (Fig. 1i), respectively. LRCNFs and HRCNFs exhibited a typical type IV adsorption/desorption isotherm with a distinct hysteresis loop, indicating the presence of micropores and mesopores [31–33]. HRCNFs had a multimodal pore width distribution, with micropores ranging from 0.78 to 1.38 nm and uniform mesopores of approximately 17.06 nm. Similarly, the pore size distribution of LRCNFs consisted of micropores ranging from 0.64 to 1.06 nm and mesopores of approximately 18.92 nm (Fig. 1j). The interconnected meso- and micro-porous structures could increase the air-dielectric interface inside the photothermal materials [34]. Furthermore, a microporous structure can construct a small-sized conductor, which can produce a strong thermal electron effect [35].

The surface roughness of CNFs was characterized by AFM. Three parallel test scans of 2 μm × 2 μm areas were performed for each sample, followed by intercepting 500 nm × 500 nm areas of three different areas on each parallel-tested CNFs to calculate the average roughness (Fig. 2a–c). As shown in Fig. 2d–f, the HRCNFs obtained by smaller-size ZIF-8 showed the highest average roughness (R_a) of 116.06 nm, which was about thrice higher than that of CNFs, forming a rich surface absorption interface. As shown in Fig. 2g, the average absorption of HRCNFs (97.62%) was found to be greater than that of LRCNFs (94.24%) and CNFs (89.78%), revealing that HRCNFs are better at capturing sunlight. To study the light absorption of the samples in the application process, the light absorption of three samples was measured in the wet state (Fig. S8). The results show that the light absorption of the samples in the wet state is better than that in the dry state. In practical applications, this would be beneficial to solar steam generation. The hierarchical porous structure increases the surface roughness of CNFs, resulting in multiple light reflections on CNFs, thus increasing light absorption. This is consistent with the phenomenon presented in Fig. 2k. HRCNFs exhibited a deeper color owing to strong light absorption. The temperature change process of the samples is shown in Fig. 2h. The maximum surface temperatures of HRCNFs, LRCNFs, and CNFs are steady at 80.0, 89.2, and 95.1°C under one sun illumination, respectively (Fig. 2j). HRCNFs had a rougher surface microstructure and could convert more light into heat, which is advantageous to water evaporation. The temperature elevation behavior of the samples was highly stable after five switching cycles under one sun illumination, among which HRCNFs exhibited the highest temperature (Fig. 2i). As a result, the HRCNF membrane was expected to significantly improve the photothermal evaporation performance of the material.

The performance of solar steam generation and water purification were further investigated experimentally. Fig. S9 depicts the assembly of a custom-built steam-generation device. Polystyrene foam was used to allow the light absorber to float on the water surface. The surface of the polystyrene foam was covered with a cotton filter paper (diameter ~ 9 cm), which was extended underwater for water transportation using the capillary effect (Fig. 3a). As shown in Fig. 3b, the evaporation rates of saline water (3.5 wt% NaCl), CNFs, LRCNFs, and HRCNFs were 0.31, 1.32, 1.64, and 1.78 kg $m^{-2} h^{-1}$, respectively. The efficiency of solar-vapor generation was an important factor in studying the water evaporation process of photothermal materials. The solar-vapor conversion efficiency of HRCNFs could reach 96.13%, which is higher than 21.06% of saline water, 73.96% of CNFs, and 86.66% of LRCNFs under one sun illumination (Fig. 3c).

As the water evaporated through HRCNFs *via* a single molecule manner, the solar steam generation device with higher-roughness HRCNFs was further applied for water purification. The concentration of Na^+ was measured before and after water purification using an inductively coupled plasma-atomic emission spectrometer (ICP-AES). Purified water was obtained by collecting condensed water in solar steam when exposed to sunlight (Fig. S10). As shown in Fig. 3d, the concentration of Na^+ in the condensation chamber decreased sharply by at least five orders of magnitude after water purification for the highly concentrated NaCl solutions (3.5, 7, 10.5, and 14 wt%). This is much lower than the salinity level defined by World Health Organization (WHO) (Na^+ < 200 mg L^{-1}) [36] and is also lower than those of the freshwater generated by commercial membrane filtration systems (Na^+: 25–300 mg L^{-1}) [37]. Additionally, simulated seawater was prepared by following the world seawater ion concentration [38], which was used to test the seawater purification effect of the evaporator. The concentrations of four primary metal ions (Na^+, Mg^{2+}, K^+, and Ca^{2+}) were also measured before and after water purification by ICP-AES. The extremely low ion concentrations in freshwater (< 0.36 mg L^{-1}) after water purification ensure that the performance of the water purification evaporator is viable (Fig. 3e). It should be noted that the salt that was deposited on the surface of HRCNF during evaporation was easily washed away by water, showing good cycle stability after 30 cycles (1 h per cycle) (Fig. 3f). To further verify the cyclic stability of HRCNFs, HRCNFs were subjected to a cyclic stability test for 80 h. After 80 h of cyclic use, the final evaporation rate of HRCNF decreased to 1.64 kg $m^{-2} h^{-1}$ (Fig. S11), which is only 7.8% lower than the initial evaporation rate (1.78 $m^{-2} h^{-1}$), evidencing good cycle stability. Under one sun illumination, the evaporation rate and conversion efficiency of HRCNFs are significantly higher than those of the two-dimensional (2D) photothermal material-based evaporators (Fig. 3g) [39–48].

The optical path diagrams of light reflection and absorption on HRCNFs, LRCNFs, and CNFs surfaces are shown in Fig. 3h. The CNF surface was smooth, and sunlight could only be reflected a few times, which is not conducive to the absorption of sunlight. In comparison, the inner walls of the grooves of the HRCNF porous structure could effectively reabsorb diffusely

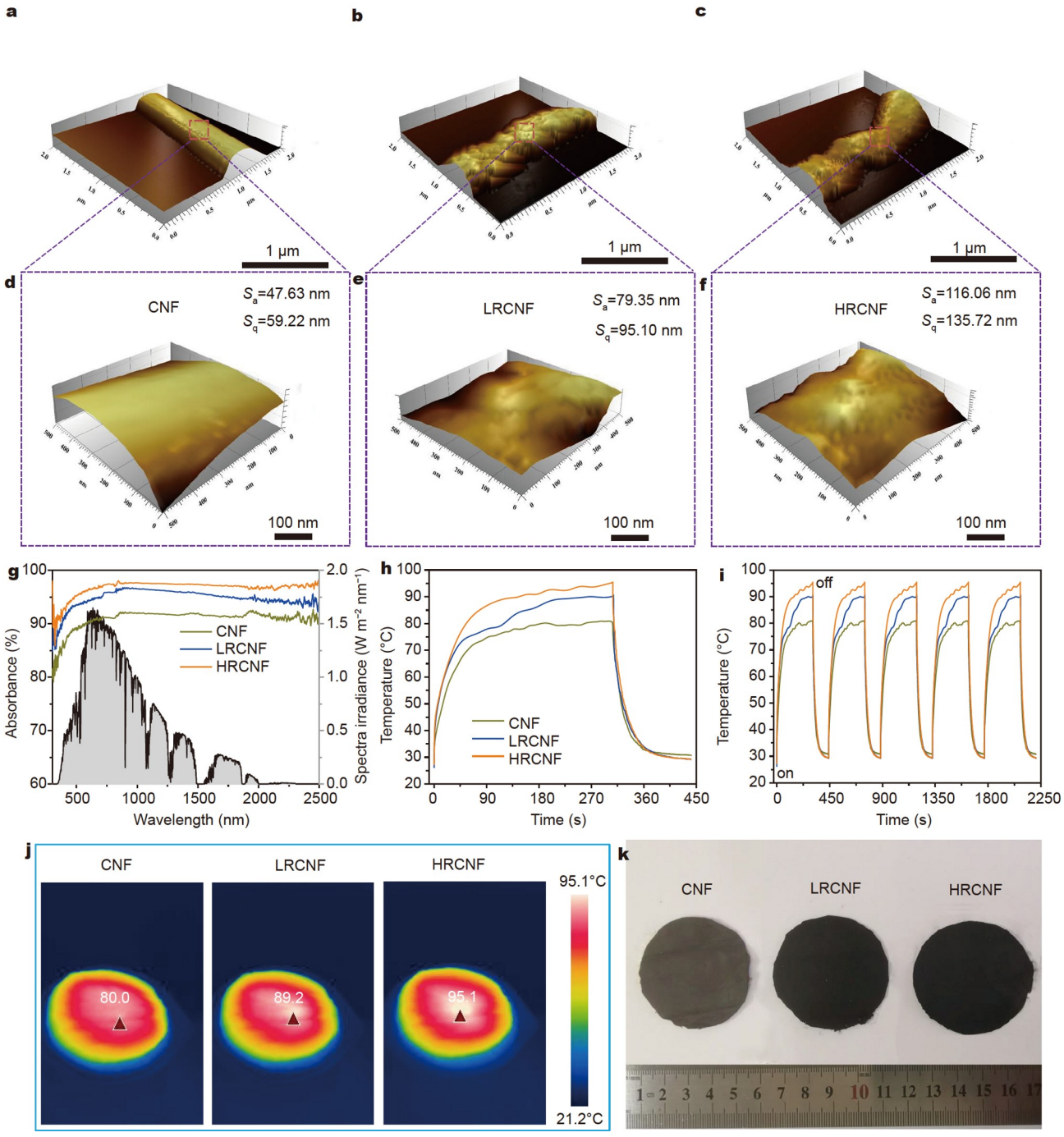

Figure 2 AFM surface morphologies of (a) CNFs, (b) LRCNFs, and (c) HRCNFs. (d–f) Screenshots of AFM images at 500 nm × 500 nm. (g) UV-vis-NIR absorption spectra of CNFs, LRCNFs, and HRCNFs. (h) Temperature response profiles of CNFs, LRCNFs, and HRCNFs under a dry state when the solar simulator is turned on and off. (i) Temperature response profiles of CNFs, LRCNFs, and HRCNFs when current is applied at an interval of 7 min. (j) IR image of CNF-, LRCNF-, and HRCNF-based devices under one sun. (k) Photographs of CNF, LRCNF, and HRCNF membranes demonstrating the color of CNF membrane deepening as the roughness increases.

reflected light, allowing energy recovery in these confined spaces. Moreover, the highest roughness of HRCNFs resulted in the largest specific surface area, resulting in the largest sunlight irradiation area received by HRCNFs. Thus, HRCNFs could convert more solar energy into heat to promote and accelerate steam escape. This also explained the better performance of solar steam generation of HRCNFs. We fitted and analyzed the relationship between solar-to-vapor efficiency and roughness. Fig. S12 shows that the solar-to-vapor efficiency has an excellent linear relationship with the roughness of CNF, indicating that even a small roughness change at the nanometer level is adequate to improve the photothermal conversion efficiency of carbon nanomaterials.

HRCNFs were ideal for water purification owing to its good

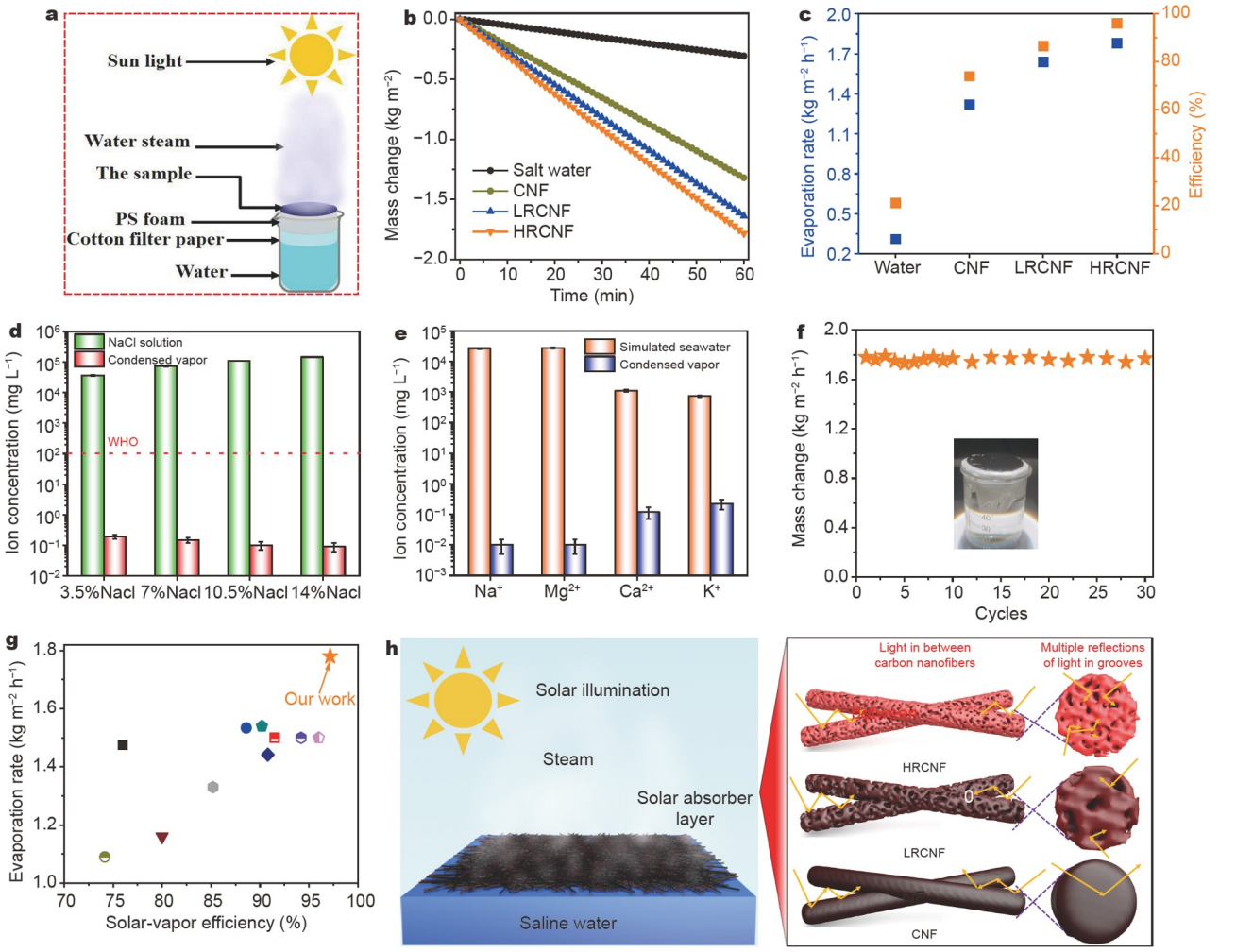

Figure 3 (a) Schematic diagram of the solar steam evaporation device. (b) Time course of water evaporation performances of saline water, CNFs, LRCNFs, and HRCNFs under one sun illumination. (c) Solar-vapor conversion efficiency and evaporation rate of saline water, CNFs, LRCNFs, and HRCNFs. (d) Na^+ concentrations in different NaCl solutions and condensed vapor after water purification. The dashed line refers to the standard for drinkable water from WHO. (e) Four main metallic solute concentrations in simulated seawater and condensed vapor after water purification. (f) Evaporation cycle performance of water purification devices with each cycle sustained for 1 h. (g) Contrast of the evaporation rate and conversion efficiency under one sun illumination between this study and the most recent reported 2D photothermal materials. (h) Schematic diagram of the microstructure of three photothermal materials, including HRCNFs, LRCNFs, and CNFs.

mechanical properties, high light absorption, and high evaporation performance. Lake water, as an alternative water resource, appeared to be a promising option for producing safe drinking water. HRCNFs (11 cm × 8.0 cm) were used to convert lake water (Donghua University, Shanghai, China) into safe drinking water. Fig. 4a shows a water purification device whose bottom is composed of a double-layer transparent porous cuboid structure (outer frame: 15 cm × 12 cm × 5.0 cm; inner frame: 12 cm × 9.0 cm × 2.0 cm) and whose top is composed of a transparent triangular structure (15 cm × 12 cm × 5.0 cm). A water tank would be formed between the outer frame and the inner frame at the bottom (water vapor would flow into the tank along the periphery after condensation). The cotton filter paper was fixed on the porous inner frame, and its function was to slowly introduce water into the photothermal materials. The photothermal materials were attached to the cotton filter paper (Fig. S13). The water purification device equipped with photothermal materials in the center of the empty foam (25 cm × 20 cm × 2.0 cm) was designed to keep the water purification device afloat on the lake (Fig. 4b). The detailed process of water evaporation has been described in the supplementary information. The purification system produced clean water under natural sunlight. As shown in Fig. 4c, the decrease in the evaporation rate was primarily determined by changes in natural solar intensity, which gradually increased from 0.62 kW m^{-2} at 8:00 am to 0.86 kW m^{-2} at 12:30 pm and then decreased to 0.50 kW m^{-2} at 18:00. Under natural sunlight, the evaporation rate went up from 0.85 kg m^{-2} h^{-1} at 8:00 am to 1.52 kg m^{-2} h^{-1} at 12:30 pm and then gradually decreased to 0.65 kg m^{-2} h^{-1} at 18:00. The HRCNF purification system produced 11.18 kg m^{-2} of clean and safe water per day, which is sufficient to meet the daily needs of 4–5 individuals [49]. It is worth noting that HRCNFs are particularly lightweight (2.28 mg cm^{-2}), making it ideal for floating on the water surface for water purification. To compare the quality of purified water to that of domestic water, the concentrations of several major ions were measured. The

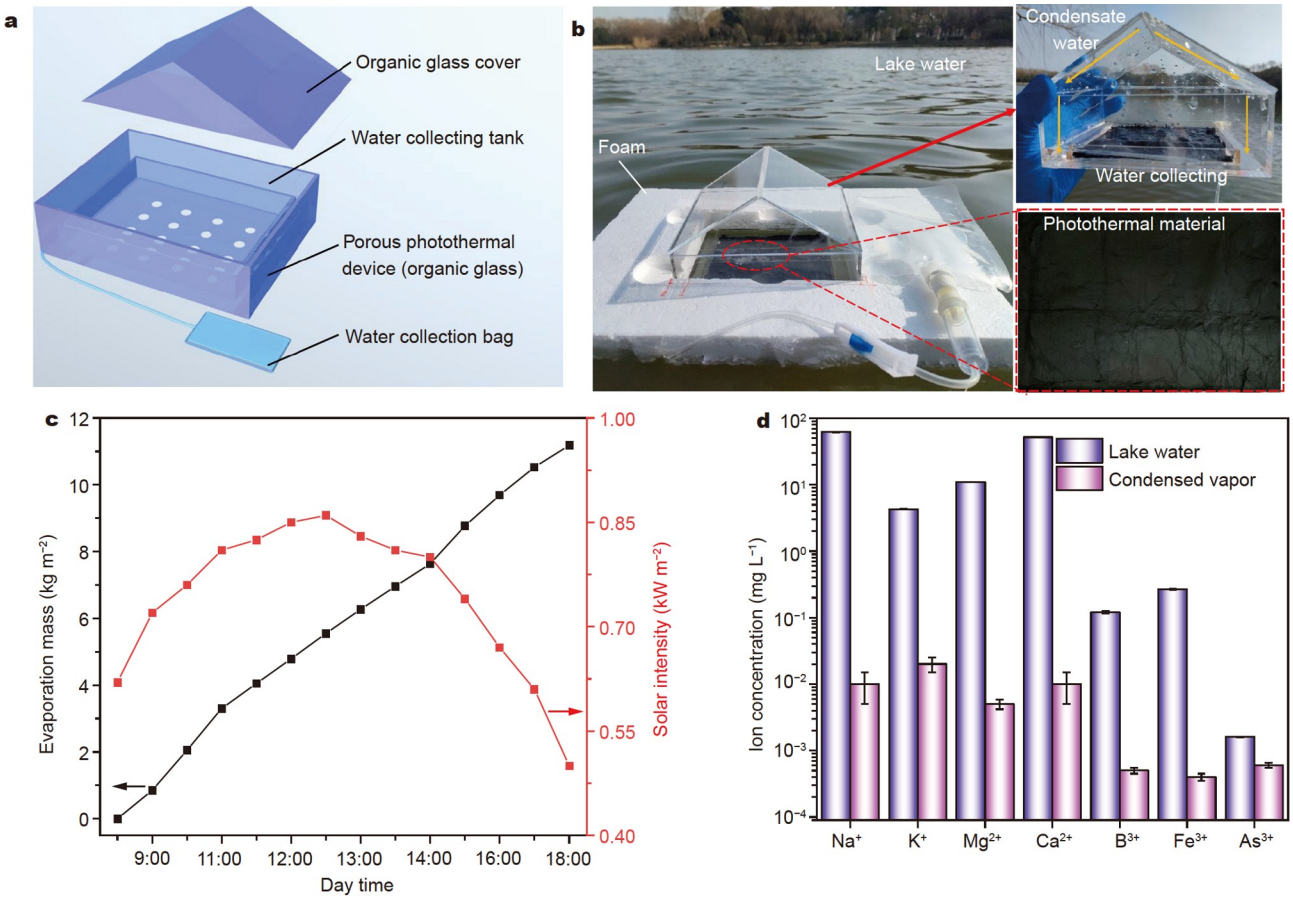

Figure 4 (a) Experimental setup of natural sunlight-driven clean water generation. (b) Photographs of the HRCNF purification system floating atop the lake. (c) Accumulated water evaporation masses and measured solar intensities at different times of the day. (d) Seven main metallic solute concentrations in lake water and condensed vapor after water purification.

concentrations of Na^+, K^+, Mg^{2+}, Ca^{2+}, B^{3+}, Fe^{3+}, and As^{3+} in the lake water before purification were found to be 62.06, 4.27, 10.99, 51.81, 0.12, 0.27, and 1.60 × 10^{-3} mg L^{-1}, respectively (Fig. 4d). The ion concentrations in freshwater were significantly reduced to <0.05 mg L^{-1} after the evaporation condensation process. These results indicate that HRCNFs have a high potential for practical solar water purification from a wide range of potable water feedstocks.

CONCLUSIONS

We proposed a facile method to enhance the light absorption properties of carbon nanomaterials by constructing multiple internal air-dielectric interfaces, which significantly improves the water evaporation performance and heat utilization. The synthesized HRCNFs outperformed LRCNFs and CNFs in terms of light absorption and water evaporation with an evaporation rate of 1.78 kg m^{-2} h^{-1} and a high solar-vapor conversion efficiency of 96.13%. Making CNFs with nanoscale roughness and hierarchical porosity can dramatically improve their intrinsic photothermal properties with absorption above 97%, reducing the reflective energy loss. The fabricated rough CNF membrane demonstrates a high rejection rate of ions (< 0.05 mg L^{-1} salt ions) and produces fresh water from the lake at a rate of 11.18 kg m^{-2} per day, which is sufficient for the daily demands of 4–5 individuals. This work provides a new idea for developing photothermal water evaporation materials with low cost and high efficiency.

Received 10 January 2023; accepted 16 February 2023; published online 9 May 2023

1 Ercin AE, Hoekstra AY. Water footprint scenarios for 2050: A global analysis. Environ Int, 2014, 64: 71–82
2 Ni G, Li G, Boriskina SV, *et al.* Steam generation under one sun enabled by a floating structure with thermal concentration. Nat Energy, 2016, 1: 16126
3 Green PA, Vörösmarty CJ, Harrison I, *et al.* Freshwater ecosystem services supporting humans: Pivoting from water crisis to water solutions. Glob Environ Change, 2015, 34: 108–118
4 Gleick PH. Water in crisis: Paths to sustainable water use. Ecol Appl, 1998, 8: 571–579
5 Xu X, Ozden S, Bizmark N, *et al.* A bioinspired elastic hydrogel for solar-driven water purification. Adv Mater, 2021, 33: 2007833
6 Liu H, Liu Y, Wang L, *et al.* Nanofiber based origami evaporator for multifunctional and omnidirectional solar steam generation. Carbon, 2021, 177: 199–206
7 Wang J, Li Y, Deng L, *et al.* High-performance photothermal conversion of narrow-bandgap Ti_2O_3 nanoparticles. Adv Mater, 2017, 29: 1603730
8 Li R, Zhang L, Shi L, *et al.* MXene Ti_3C_2: An effective 2D light-to-heat conversion material. ACS Nano, 2017, 11: 3752–3759
9 Zhou Z, Wang X, Zhang H, *et al.* Activating layered metal oxide nanomaterials *via* structural engineering as biodegradable nanoagents for

photothermal cancer therapy. Small, 2021, 17: 2007486
10 Chen F, Yang D, Shen H, *et al.* Hydrothermal synthesis of novel rhombic dodecahedral SnS nanocrystals for highly efficient photothermal therapy. Chem Commun, 2019, 55: 2789–2792
11 He M, Dai H, Liu H, *et al.* High-performance solar steam generator based on polypyrrole-coated fabric *via* 3D macro- and microstructure design. ACS Appl Mater Interfaces, 2021, 13: 40664–40672
12 Ito Y, Tanabe Y, Han J, *et al.* Multifunctional porous graphene for high-efficiency steam generation by heat localization. Adv Mater, 2015, 27: 4302–4307
13 Li Y, Gao T, Yang Z, *et al.* Graphene oxide-based evaporator with one-dimensional water transport enabling high-efficiency solar desalination. Nano Energy, 2017, 41: 201–209
14 Wang F, Wei D, Li Y, *et al.* Chitosan/reduced graphene oxide-modified spacer fabric as a salt-resistant solar absorber for efficient solar steam generation. J Mater Chem A, 2019, 7: 18311–18317
15 Ma X, Fang W, Guo Y, *et al.* Hierarchical porous SWCNT stringed carbon polyhedrons and PSS threaded MOF bilayer membrane for efficient solar vapor generation. Small, 2019, 15: 1900354
16 Xu W, Hu X, Zhuang S, *et al.* Flexible and salt resistant Janus absorbers by electrospinning for stable and efficient solar desalination. Adv Energy Mater, 2018, 8: 1702884
17 Zhang Q, Ye Q, Zhang Y, *et al.* High efficiency solar interfacial evaporator for seawater desalination based on high porosity loofah sponge biochar. Sol Energy, 2022, 238: 305–314
18 Yan J, Xiao W, Chen L, *et al.* Superhydrophilic carbon nanofiber membrane with a hierarchically macro/meso porous structure for high performance solar steam generators. Desalination, 2021, 516: 115224
19 Zhu M, Li Y, Chen G, *et al.* Tree-inspired design for high-efficiency water extraction. Adv Mater, 2017, 29: 1704107
20 Ren H, Tang M, Guan B, *et al.* Hierarchical graphene foam for efficient omnidirectional solar-thermal energy conversion. Adv Mater, 2017, 29: 1702590
21 Yang ZP, Ci L, Bur JA, *et al.* Experimental observation of an extremely dark material made by a low-density nanotube array. Nano Lett, 2008, 8: 446–451
22 Zhao F, Guo Y, Zhou X, *et al.* Materials for solar-powered water evaporation. Nat Rev Mater, 2020, 5: 388–401
23 Inagaki M, Yang Y, Kang F. Carbon nanofibers prepared *via* electrospinning. Adv Mater, 2012, 24: 2547–2566
24 Lee YR, Jang MS, Cho HY, *et al.* ZIF-8: A comparison of synthesis methods. Chem Eng J, 2015, 271: 276–280
25 Hu X, Xu W, Zhou L, *et al.* Tailoring graphene oxide-based aerogels for efficient solar steam generation under one sun. Adv Mater, 2017, 29: 1604031
26 Zhang Y, Yuan S, Feng X, *et al.* Preparation of nanofibrous metal-organic framework filters for efficient air pollution control. J Am Chem Soc, 2016, 138: 5785–5788
27 Xu Z, Li Z, Jiang Y, *et al.* Recent advances in solar-driven evaporation systems. J Mater Chem A, 2020, 8: 25571–25600
28 Wang X, Liu Q, Wu S, *et al.* Multilayer polypyrrole nanosheets with self-organized surface structures for flexible and efficient solar-thermal energy conversion. Adv Mater, 2019, 31: 1807716
29 Han X, Besteiro LV, Koh CSL, *et al.* Intensifying heat using MOF-isolated graphene for solar-driven seawater desalination at 98% solar-to-thermal efficiency. Adv Funct Mater, 2021, 31: 2008904
30 Liu X, Cao XE, Liu Y, *et al.* Branched multiphase TiO_2 with enhanced photoelectrochemical water splitting activity. Int J Hydrogen Energy, 2018, 43: 21365–21373
31 Li M, Yang W, Li J, *et al.* Porous layered stacked $MnCo_2O_4$ cubes with enhanced electrochemical capacitive performance. Nanoscale, 2018, 10: 2218–2225
32 Niu S, Wang Z, Zhou T, *et al.* A polymetallic metal-organic framework-derived strategy toward synergistically multidoped metal oxide electrodes with ultralong cycle life and high volumetric capacity. Adv Funct Mater, 2017, 27: 1605332
33 Sing KSW. Reporting physisorption data for gas/solid systems with special reference to the determination of surface area and porosity (Recommendations 1984). Pure Appl Chem, 1985, 57: 603–619
34 Xu X, Tan H, Wang Z, *et al.* Extraordinary capacitive deionization performance of highly-ordered mesoporous carbon nano-polyhedra for brackish water desalination. Environ Sci-Nano, 2019, 6: 981–989
35 Wang H, Du A, Ji X, *et al.* Enhanced photothermal conversion by hot-electron effect in ultrablack carbon aerogel for solar steam generation. ACS Appl Mater Interfaces, 2019, 11: 42057–42065
36 Santé O. Guidelines for Drinking-water Quality. Geneva: World Health Organization, 1996
37 Stevens DM, Shu JY, Reichert M, *et al.* Next-generation nanoporous materials: Progress and prospects for reverse osmosis and nanofiltration. Ind Eng Chem Res, 2017, 56: 10526–10551
38 Zhao J, Yu K, Hu Y, *et al.* Discharge behavior of Mg-4wt%Ga-2wt%Hg alloy as anode for seawater activated battery. Electrochim Acta, 2011, 56: 8224–8231
39 Li A, Xiong J, Liu Y, *et al.* Fiber-intercepting-particle structured MOF fabrics for simultaneous solar vapor generation and organic pollutant adsorption. Chem Eng J, 2022, 428: 131365
40 Ying P, Ai B, Hu W, *et al.* A bio-inspired nanocomposite membrane with improved light-trapping and salt-rejecting performance for solar-driven interfacial evaporation applications. Nano Energy, 2021, 89: 106443
41 Ren L, Yi X, Yang Z, *et al.* Designing carbonized loofah sponge architectures with plasmonic Cu nanoparticles encapsulated in graphitic layers for highly efficient solar vapor generation. Nano Lett, 2021, 21: 1709–1715
42 Peng Y, Wang Y, Li W, *et al.* Bio-inspired vertically aligned polyaniline nanofiber layers enabling extremely high-efficiency solar membrane distillation for water purification. J Mater Chem A, 2021, 9: 10678–10684
43 Ma Q, Yin P, Zhao M, *et al.* MOF-based hierarchical structures for solar-thermal clean water production. Adv Mater, 2019, 31: 1808249
44 Xu N, Hu X, Xu W, *et al.* Mushrooms as efficient solar steam-generation devices. Adv Mater, 2017, 29: 1606762
45 Sun H, Li Y, Li J, *et al.* Facile preparation of a carbon-based hybrid film for efficient solar-driven interfacial water evaporation. ACS Appl Mater Interfaces, 2021, 13: 33427–33436
46 Xu Y, Ma J, Liu D, *et al.* Origami system for efficient solar driven distillation in emergency water supply. Chem Eng J, 2019, 356: 869–876
47 Zou Y, Chen X, Yang P, *et al.* Regulating the absorption spectrum of polydopamine. Sci Adv, 2020, 6: eabb4696
48 Li Z, Ma X, Chen D, *et al.* Polyaniline-coated MOFs nanorod arrays for efficient evaporation-driven electricity generation and solar steam desalination. Adv Sci, 2021, 8: 2004552
49 Liu Z, Zhou Z, Wu N, *et al.* Hierarchical photothermal fabrics with low evaporation enthalpy as heliotropic evaporators for efficient, continuous, salt-free desalination. ACS Nano, 2021, 15: 13007–13018

Acknowledgements This work was supported by the Chang Jiang Scholars Program and the Innovation Program of Shanghai Municipal Education Commission (2019-01-07-00-03-E00023), the National Natural Science Foundation of China (52202218, 62171116 and 51973027), DHU Distinguished Young Professor Program, Shanghai Committee of Science and Technology (22ZR1401000) and Shanghai Pujiang Program (21PJ1400200).

Author contributions Luo Q conducted the experiments, analyzed the data and wrote the original draft with support from Yang Y and Wang K. Qin X, Yu J, and Wang R supervised the project. Ji D conceived the idea, supervised the work and revised the draft. All authors contributed to the general discussion.

Conflict of interest The authors declare that they have no conflict of interest.

Supplementary information Supporting data are available in the online version of the paper.

Qingliang Luo is a PhD candidate at the School of Textiles, Donghua University, China. His research interests include functional electrospinning membranes, single-atom catalysis and flexible zinc air batteries.

Rongwu Wang is currently a professor at the College of Textiles, Donghua University, China. He received his PhD degree from the College of Textiles, Donghua University in 2008. His current research interest focuses on the structural analysis and design of non-nonwovens.

Dongxiao Ji is a distinguished young professor at Donghua University, China. He received his MS and PhD degrees in textile science and engineering from Donghua University in 2012 and 2018, respectively. Then, he worked as a research fellow at the Nanofiber Research Center of National University of Singapore. Dr. Ji is committed to the research of large-scale electrospinning technology for nanofibers and nanoparticles and their applications in energy and smart systems.

分级多孔碳纳米纤维用于高效太阳能驱动水净化

罗清亮[1], 羊燚[1], 汪康康[1], 俞建勇[2], 王荣武[1*], 季东晓[1*], 覃小红[1]

摘要 碳材料通常用于太阳能水蒸发，因为它们可以吸收宽带光并有效地产生热量. 然而，具有光滑表面的传统碳材料受到大约10%的中等反射的限制，损失了反射能量. 在此，我们提出了一种多界面策略，以提高碳纳米纤维(CNFs)的固有光吸收，从而实现更高效的太阳能驱动水净化. 通过简单的牺牲模板方法，在CNFs中引入分级孔来构建多个界面得到高表面粗糙度碳纳米纤维(HPCNFs). 由于高表面粗糙度和源自分级孔的丰富内部空气介电界面，HPCNFs在宽带光(300–2500 nm)吸收显著改善，高达97.62%，这使得在1个太阳光照下的太阳光转换为蒸汽的效率达到96.13%，蒸发率高达1.78 kg m^{-2} h^{-1}，超过了大多数相关的纯碳材料. 当用于太阳能水蒸发脱盐时，HPCNF膜表现出对离子的高度排斥(< 0.05 mg L^{-1}盐离子)，并以每天11.18 kg m^{-2}的速率从湖中产生淡水，足以满足4–5个人的日常需求. 这项工作为高效碳基太阳能水蒸发材料的设计提供了一种简便策略.